

Living with Neighbors. III. Scrutinizing the Spin–Orbit Alignment of Interacting Dark Matter Halo Pairs

SUNG-HO AN,^{1,2} JUHAN KIM,³ JUN-SUNG MOON,^{1,2} AND SUK-JIN YOON^{1,2}

¹*Department of Astronomy, Yonsei University, Seoul 03722, Republic of Korea*

²*Center for Galaxy Evolution Research, Yonsei University, Seoul 03722, Republic of Korea*

³*Center for Advanced Computation, Korea Institute for Advanced Study, Seoul 02455, Republic of Korea*

(Revised May 1, 2022)

ABSTRACT

We present that the spin–orbit alignment (SOA; i.e., the angular alignment between the spin vector of a halo and the orbital angular momentum vector of its neighbor) provides an important clue to how galactic angular momenta develop. In particular, we identify virial-radius-wise contact halo pairs with mass ratios from 1/3 to 3 in a set of cosmological N -body simulations, and divide them into merger and flyby subsamples according to their total (kinetic+potential) energy. In the spin–orbit angle distribution, we find a significant SOA in that $75.0 \pm 0.6\%$ of merging neighbors and $58.7 \pm 0.6\%$ of flybying neighbors are on the prograde orbit. The overall SOA of our sample is mainly driven by fast-rotating halos, corroborating that a well-aligned interaction spins a halo faster. More interestingly, we find for the first time a strong number excess of nearly perpendicular but still prograde interactions ($\sim 75^\circ$) in the spin–orbit angle distribution for both the merger and flyby cases. Such prograde-polar interactions predominate for slow-rotating halos, testifying that misaligned interactions reduce the halos’ spin. The frequency of the prograde-polar interactions correlates with the halo mass, yet anticorrelates with the large-scale density. This instantly invokes the spin-flip phenomenon that is conditional on the mass and environment. The prograde-polar interaction will soon flip the spin of a slow-rotator to align with its neighbor’s orbital angular momentum. Finally, we propose a scenario that connects the SOA to the ambient large-scale structure based on the spin-flip argument.

Keywords: Galaxy interactions (600), Galaxy encounters (592), Galaxy dark matter halos (1880), Large-scale structure of the universe (902), Cosmic web (330), Galaxy kinematics (602), Dark matter (353), N -body simulations (1083)

1. INTRODUCTION

Recent observations have revealed that the halo spin is associated with the large-scale structure (LSS). The spin–LSS alignment arises from the tidal torque of the ambient anisotropic matter distribution exerted on the internal, rotational angular momentum of a galaxy (the tidal torque theory; Peebles 1969; Vitvitska et al. 2002; Peirani et al. 2004; Bett et al. 2007, 2010; Stewart et al. 2013; Zavala et al. 2016; Zjupa & Springel 2017). Simulations have shown that in filaments, for instance, the less (more) massive halos tend to have a spin direction par-

allel (perpendicular) to the filamentary spine (Aragón-Calvo et al. 2007; Hahn et al. 2007; Codis et al. 2015; Laigle et al. 2015; Wang & Kang 2017). Observations have shown that this spin–LSS alignment also holds true for galaxies (Tempel & Libeskind 2013; Blue Bird et al. 2020; Welker et al. 2020; see also Krolewski et al. 2019). On the other hand, recent studies have reported the link between the spin (and the shape) of centrals and the spatial distribution of their satellites. Such spin–satellite alignment is found among dark matter halos (Wang et al. 2014; Kang & Wang 2015) and among galaxies (Brainerd 2005; Yang et al. 2006; Agustsson & Brainerd 2010; Dong et al. 2014; Tempel et al. 2015; Velliscig et al. 2015; Shao et al. 2016; Wang et al. 2018b). The alignment depends on the mass (Velliscig et al. 2015),

morphology (Wang et al. 2010), color of central galaxies (Wang et al. 2018b), and color of satellites (Dong et al. 2014). The spin–satellite alignment indicates that the galaxy (or halo) spin is regulated by the tidal interaction. Taking the two types of alignments together, it has been suggested that the angular momentum of a galaxy evolves with nonlinear events such as mergers and accretions along the local LSS (Porciani et al. 2002; Vitvitska et al. 2002; Peirani et al. 2004; Hetznecker & Burkert 2006; Hahn et al. 2007; Cervantes-Sodi et al. 2010; Stewart et al. 2013; Rodriguez-Gomez et al. 2017; Peng & Renzini 2020).

Motivated by the spin–LSS and spin–satellite alignments, we explore the alignment between the spin of a halo and the orbital angular momentum of its comparable-mass neighbor, which we refer to the “spin–orbit alignment (SOA).” Our working hypotheses are (a) that interacting neighbors came preferentially along the LSS (Wang & Kang 2018) and thus their orbital angular momenta reflect the direction of surrounding matter flow, and (b) that the neighbor’s orbital angular momentum can be converted into the internal angular momentum of the central galaxy (e.g., Aubert et al. 2004; Bailin & Steinmetz 2005). Previous studies, which dealt with smaller satellites only, found that the mean orbital angular momentum of satellites has no correlation with the spin of the central galaxy (e.g., Herbert-Fort et al. 2008; Hwang & Park 2010). Some studies found no spin–spin alignment for interacting pairs composed of two comparable-mass galaxies (Cervantes-Sodi et al. 2010; Buxton & Ryden 2012; Lee 2012; Mesa et al. 2014). However, the correlation between the spin of a galaxy and the orbital angular momentum of its comparable-mass neighbor has not yet been explored. We expect that dark matter halo pairs will display the SOA as the halo spin becomes faster within the strong tidal field (Wang et al. 2011) such as the pair system (Johnson et al. 2019; see also Cervantes-Sodi et al. 2010). This work focuses on the SOA in the case of interactions with the comparable-mass companions. Using a set of cosmological N -body simulations, we intend to address the question of which physical parameter dominantly influences the direction and magnitude of the halo spin. To this end, we measure the SOA of merging and flybying neighbors and examine a dependence of the alignment on the halo mass, large-scale environment, pairwise distance, halo triaxiality, and halo spin parameter.

The present series of papers investigate both observationally and theoretically the impact of interacting neighbor galaxies (or halos) on the galactic properties. Moon et al. (2019, Paper I) revealed how strongly the nearest neighbor affects the star formation activity of a

galaxy using a comprehensive galaxy pair catalog from the Sloan Digital Sky Survey (York et al. 2000). An et al. (2019, Paper II), using a set of cosmological N -body simulations, found that flyby-type interactions substantially outnumber merger-type interactions toward $z = 0$, and that the flyby contributes to the galactic evolution more significantly than ever at the present epoch—especially for lower-mass halos and in denser environments. This third paper is an extension of Paper II, exploiting the same dataset used in that work, and attempts to understand the build-up process of galactic angular momentum via the SOA of mergers and flybys.

It is fair to mention a possible caveat regarding this study. The work focuses on the SOA of dark matter halos rather than galaxies. The spin vector of dark matter halos are reported to be somewhat misaligned with the spin vector of baryonic components (so-called galaxy–halo misalignment), but the mean angle offset ($25^\circ \sim 50^\circ$; Bailin & Steinmetz 2005; Shao et al. 2016; Chisari et al. 2017) is smaller than the offset (57°) expected from the random distribution. The degree of galaxy–halo misalignment depends on the halo and galaxy properties (Bailin et al. 2005; Velliscig et al. 2015; Ganeshaiah Veena et al. 2019). Many studies have shown that the tidal interaction significantly affect the halo (galaxy) spin (Hetznecker & Burkert 2006; Cervantes-Sodi et al. 2010; Wang et al. 2011; Johnson et al. 2019). This implies that the SOA makes the present galaxy–halo alignment stronger, similarly to the effect of satellite galaxies on the galaxy–halo alignment for their central galaxy (Shao et al. 2016). Therefore, despite the caveat, we will assume that the halo spin represents the galaxy spin, and discuss implications for our results later.

This paper is organized as follows. Section 2 describes our simulations and the measurement method of the SOA. Section 3 shows the spin–orbit angle distributions and estimates their dependence on various parameters. In Section 4 we discuss the physical causes and implications of the features of the spin–orbit angle distributions, linking it to the LSS. We summarize our results in Section 5.

2. DATA AND ANALYSIS

2.1. Halo Pair Sample and Subsamples

We perform a series of the cosmological N -body simulations using the parallel tree particle-mesh code, GOTPM (Grid-of-Oct-Tree-Particle-Mesh; Dubinski et al. 2004). There are 11 simulations in total, each with the same mass resolution of $M_p = 1.55 \times 10^8 h^{-1} M_\odot$, but with boxsizes of $(64 h^{-1} \text{Mpc})^3$ for 10 simulations and $(128 h^{-1} \text{Mpc})^3$ for one. All simulations are conducted in the WMAP 9-year cosmology (Bennett

et al. 2013) and use different random seeds to take into account the cosmic variance (see Paper II for details).

We employ ROCKSTAR (Robust Overdensity Calculation using K-Space Topologically Adaptive Refinement; Behroozi et al. 2013) halo-finding algorithm to build a halo catalog. In the 11 simulations, we choose the target halos with a halo mass range from $10^{10.8} h^{-1} M_\odot$ to $10^{13.0} h^{-1} M_\odot$ (a total of 263,256 halos at $z=0$) and identify the halos with interacting neighbors using the same criteria with Paper II. In short, the mass ratio range is from 1/3 to 3, and the distance between the target halo and its neighbor should be smaller than the sum of the virial radii of two halos ($d_{12} < R_{1,\text{vir}} + R_{2,\text{vir}}$). In this study, one target halo can have multiple neighbors, and we count all the neighbors with different orbital configurations. The total number of paired neighbors is defined by

$$N_{\text{sample}} \equiv \sum_i^{N_{\text{target}}} N_{\text{neigh},i}, \quad (1)$$

where $N_{\text{neigh},i}$ is the number of neighbors that belong to the i th target halo. At $z=0$, 36,092 interacting neighbors (N_{sample}) in 30,392 target halos (N_{target}) satisfy the imposed mass ratio and distance criteria (about 1.2 interacting neighbors per one target halo). The number fraction of our multiple interactions is five times higher than the observation by Darg et al. (2011), due to our distance criterion ($\sim 300 h^{-1} \text{kpc}$) being longer than theirs (30 kpc).

Next, we break the pair sample according to the halo mass, environment, and total energy of the pair system. First, based on the virial mass, there are three subsamples: the low-mass halos ($M_{\text{L10}} \equiv \log_{10}(M_{\text{target}}/h^{-1} M_\odot) \in [10.8, 11.0]$), the intermediate-mass halos ($M_{\text{L10}} \in [11.0, 11.5]$), and the high-mass halos ($M_{\text{L10}} \in [11.5, 13.0]$). Next, we define the environmental parameter (Φ_{Env}) as the percentile rank of the total mass of halos that are more massive than $10^{9.8} h^{-1} M_\odot$ within a comoving radius of $5 h^{-1} \text{Mpc}$. The interacting neighbors are divided into three subsamples: the low-density environment ($0 < \Phi_{\text{Env}} \leq 35$), the intermediate-density environment ($35 < \Phi_{\text{Env}} \leq 65$), and the high-density environment ($65 < \Phi_{\text{Env}} \leq 100$). We label the subsamples with S_{ij} ; the first and second subscripts vary from 1 to 3 with increasing mass and environmental parameter, respectively. Finally, based on the total energy (kinetic plus potential; E_{12}), we classify the interacting neighbors into mergers ($E_{12} < \Delta E$) and flybys ($E_{12} \geq \Delta E$), where ΔE is the capture criterion of Gnedin (2003), which gave an analytic solution of the energy loss during encounter via a calculation of the velocity drag induced by the dynamical friction. Some

pairs with positive energy could ultimately be merged (see Equations 4 and 5 of Paper II for details). Now we have a total of 18 subsamples for the analysis of the SOA.

2.2. Spin-Orbit Angle Measurements

To quantify the SOA, we first measure the angle (θ_{SL}) between the spin vector of a target halo (\mathbf{S}) and the orbital angular momentum vector of its neighbor (\mathbf{L}). Prior to the vector measurement, we take into account the definition of position and velocity of a halo, to minimize the effect of the tidally stripped structures during the contact interaction. The halo's position and velocity are defined by using the bound member particles in the innermost region (about 10 % of the halo radius; see Behroozi et al. 2013 for details). The vector \mathbf{S} is a sum of orbital angular momenta of bound member particles in the target halo. The vector $\mathbf{L} (\equiv \mathbf{d}_{12} \times \mathbf{V}_{12})$ is a cross product of a center position of the neighbor halo from the target halo center (\mathbf{d}_{12}) and the relative velocity (\mathbf{V}_{12}) with the consideration of the Hubble flow.

The next step is to quantify the strength of the SOA and its error, by adopting the method of Yang et al. (2006). For the analysis of three-dimensional alignment, we measure the directional cosine ($\mu_{\text{SL}} \equiv \cos \theta_{\text{SL}}$) between the spin of target halo and the orbital angular momentum of its neighbor, and we take μ_{SL} (not θ_{SL} itself) as the spin-orbit angle. The relative frequency of the interacting neighbors to the uniform distribution at a given spin-orbit angle (μ_{SL}) is then defined as

$$n(\mu_{\text{SL}}) \equiv \frac{N(\mu_{\text{SL}})}{\langle N_{\text{rand}}(\mu_{\text{SL}}) \rangle}, \quad (2)$$

where $N(\mu_{\text{SL}})$ is the number of neighbors at the given μ_{SL} and $\langle N_{\text{rand}}(\mu_{\text{SL}}) \rangle$ is a mean value of $N_{\text{rand}}(\mu_{\text{SL}})$ obtained from 100 random isotropic samples with the same number of neighbors. If there is no alignment, $n(\mu_{\text{SL}}) = 1$. If $n(\mu_{\text{SL}})$ is greater than 1, the halo spin is preferentially aligned with the orbital angular momentum of the neighbor at μ_{SL} . The angular alignment for $0 < \mu_{\text{SL}} \leq 1$ is dubbed the “prograde” alignment, and that for $-1 \leq \mu_{\text{SL}} < 0$ is dubbed the “retrograde” alignment.

3. RESULTS

3.1. Spin-Orbit Angle Distribution

We examine the SOA for various mass and environment subsamples at $z=0$. Figure 1 shows the spin-orbit angle distribution for the interacting neighbors. In all subsamples, the prograde alignment is noticeable while the retrograde alignment is insignificant. Moreover, the amplitude of prograde alignment shows the systematic

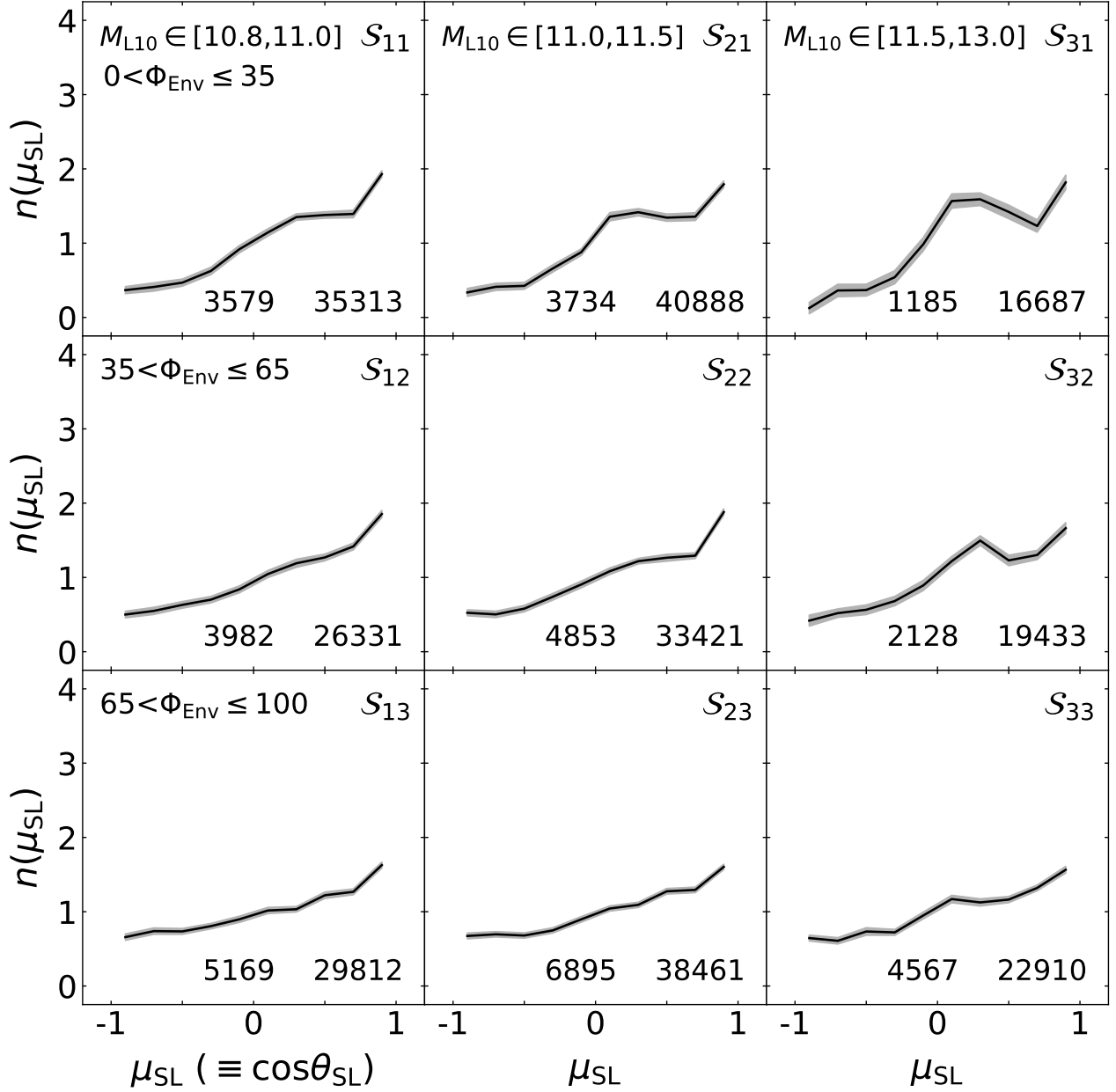


Figure 1. Spin-orbit angle (μ_{SL}) distribution for interacting neighbors (black lines) at the given halo mass (columns) and given environmental parameter (rows). Each subsample is labeled as S_{ij} ; the first and second subscripts increase from 1 to 3 with the mass and the environmental parameter, respectively. Error (shaded region) is 1σ scatter obtained from 100 random generations. At the bottom of each panel, we leave numbers of the interacting neighbors (left) and total halos (right) of each subsample (S_{ij}).

trend across S_{ij} subsamples. Table 1 provides the alignment amplitudes at $0 < \mu_{\text{SL}} < 1$ (on the prograde orbit). To simply describe the amplitudes, we define n_α by

$$n_\alpha \equiv n(\alpha - 0.1 < \mu_{\text{SL}} < \alpha + 0.1). \quad (3)$$

In Figure 1 and Table 1, the values of $n_{0.1}$ and $n_{0.3}$ tend to increase with the halo mass (i increases) whereas the trend of $n_{0.9}$ is reversed. The values of n_α decrease

with environment (j increases), except for $n_{0.7}$. For all interacting neighbors, the mass dependence is twofold but the environmental dependence is monotonic.

Our results showing a preference for the prograde interaction are consistent with previous findings from simulations (L’Huillier et al. 2017) and observations (Lee et al. 2019a,b). Lee et al. (2019b) found a coherence between the galaxy spin and neighbors’ motion even

Table 1. Values of n_α in the Subsamples of Figure 1.

Sample	All Interacting Neighbors				
	$n_{0.1}$	$n_{0.3}$	$n_{0.5}$	$n_{0.7}$	$n_{0.9}$
\mathcal{S}_{11}	1.14 ± 0.05	1.35 ± 0.04	1.38 ± 0.04	1.39 ± 0.05	1.93 ± 0.04
\mathcal{S}_{12}	1.05 ± 0.05	1.19 ± 0.05	1.27 ± 0.05	1.42 ± 0.05	1.85 ± 0.05
\mathcal{S}_{13}	1.02 ± 0.04	1.03 ± 0.04	1.22 ± 0.04	1.27 ± 0.04	1.63 ± 0.04
\mathcal{S}_{21}	1.36 ± 0.06	1.42 ± 0.05	1.34 ± 0.05	1.36 ± 0.05	1.79 ± 0.04
\mathcal{S}_{22}	1.08 ± 0.04	1.22 ± 0.04	1.27 ± 0.05	1.29 ± 0.04	1.88 ± 0.04
\mathcal{S}_{23}	1.04 ± 0.03	1.09 ± 0.04	1.27 ± 0.04	1.29 ± 0.04	1.60 ± 0.04
\mathcal{S}_{31}	1.57 ± 0.10	1.59 ± 0.09	1.42 ± 0.09	1.23 ± 0.08	1.82 ± 0.10
\mathcal{S}_{32}	1.22 ± 0.06	1.50 ± 0.06	1.23 ± 0.07	1.30 ± 0.06	1.66 ± 0.07
\mathcal{S}_{33}	1.17 ± 0.05	1.12 ± 0.05	1.16 ± 0.04	1.32 ± 0.04	1.56 ± 0.05

Notes. Values of n_α are defined by $n(\alpha - 0.1 < \mu_{\text{SL}} < \alpha + 0.1)$ in Equation 2. The error is calculated from 100 random generations. In the \mathcal{S}_{ij} sample, the first and second indices increase with the halo mass and the environmental parameter, respectively.

up to a scale of several megaparsecs (800 kpc in Lee et al. 2019a), beyond our distance criterion (on average $300 h^{-1} \text{kpc}$). The prograde alignment seems to be predicted from two facts: one is that the halo spin is associated with the local LSS (Aragón-Calvo et al. 2007; Codis et al. 2012; Tempel & Libeskind 2013; Forero-Romero et al. 2014; Zhang et al. 2015; Wang et al. 2018a) and the other is that the satellites are accreted along the local LSS (Libeskind et al. 2005; Kang & Wang 2015).

For a further analysis, in Figure 2, we compare the spin-orbit angle distributions between neighbors that are merging (red lines) versus those that are flybying (blue). Tables 2 and 3 give the n_α of subsamples, similarly to Table 1. The merger samples typically tend to have a higher frequency than the flyby samples at $0 \lesssim \mu_{\text{SL}} \leq 1$, showing the strong prograde alignment. On average, the merging neighbors at $\mu_{\text{SL}} \simeq 0.9$ have $\sim 70\%$ stronger alignment than the flybying neighbors: $n_{0.9} \simeq 2.2$ and 1.3 for the merger and flyby samples, respectively. We attribute the stronger prograde alignment for the merging neighbors to their duration of interaction being longer than that of the flybying neighbors.

The merger samples show a bit stronger prograde alignment for lower-mass halos and in denser environments. The value of $n_{0.9}$ decreases with increasing halo mass by a factor of 1.3, and it increases with the environmental density by a factor of 1.1. The variation of the SOA among subsamples seems to reflect the tidal effect, which depends on the halo mass and environment. The angular momentum of a less massive halo is more susceptible to external perturbation. The dense environment provides stronger tidal force (Shi et al. 2015), and thus it is easy for the halo spin to be tilted (Wang & Kang 2018). In contrast, the spin-orbit angle distribu-

tions for the flybying neighbors are more or less fixed regardless of the mass and environment. This is because the flybying neighbors mainly have a shorter interaction duration to exchange the tidal torque, due to the higher relative velocity (Paper II).

Interestingly enough, the amplitude of the spin-orbit angle distribution is not monotonic. For the merging neighbors, there is an unexpected bump in the distribution at $0.0 < \mu_{\text{SL}} < 0.5$. For the flybying neighbors, there is a transition of the slope at $\mu_{\text{SL}} = 0$ getting shallower at $\mu_{\text{SL}} > 0$ in all subsamples. The number excess of the prograde-polar interactions ($0.0 < \mu_{\text{SL}} < 0.5$) becomes stronger as the halo mass increases and the environmental parameter decreases. This implies that the spin directions of their target halos will be inclined toward the orbital angular momenta of interacting neighbors soon, which will be addressed in Section 3.3.

3.2. Prograde Fraction

Figure 3 shows the prograde fraction as a function of the halo mass (top panels) and the environmental parameter (bottom), respectively. Each subsample is divided into eight bins that have the same number of interacting neighbors, instead of the number of target halos, because one target halo can have multiple neighbors. We measure the prograde fraction (f_{prog}) in order to quantitatively examine the mass and environmental dependence of the prograde alignment. The prograde fraction is defined as

$$f_{\text{prog}} (\%) \equiv \frac{N_{\text{neigh}}(\mu_{\text{SL}} > 0)}{N_{\text{neigh}}(\text{total})} \times 100, \quad (4)$$

where $N_{\text{neigh}}(\mu_{\text{SL}} > 0)$ is the number of interacting neighbors on the prograde orbit ($\mu_{\text{SL}} > 0$) and

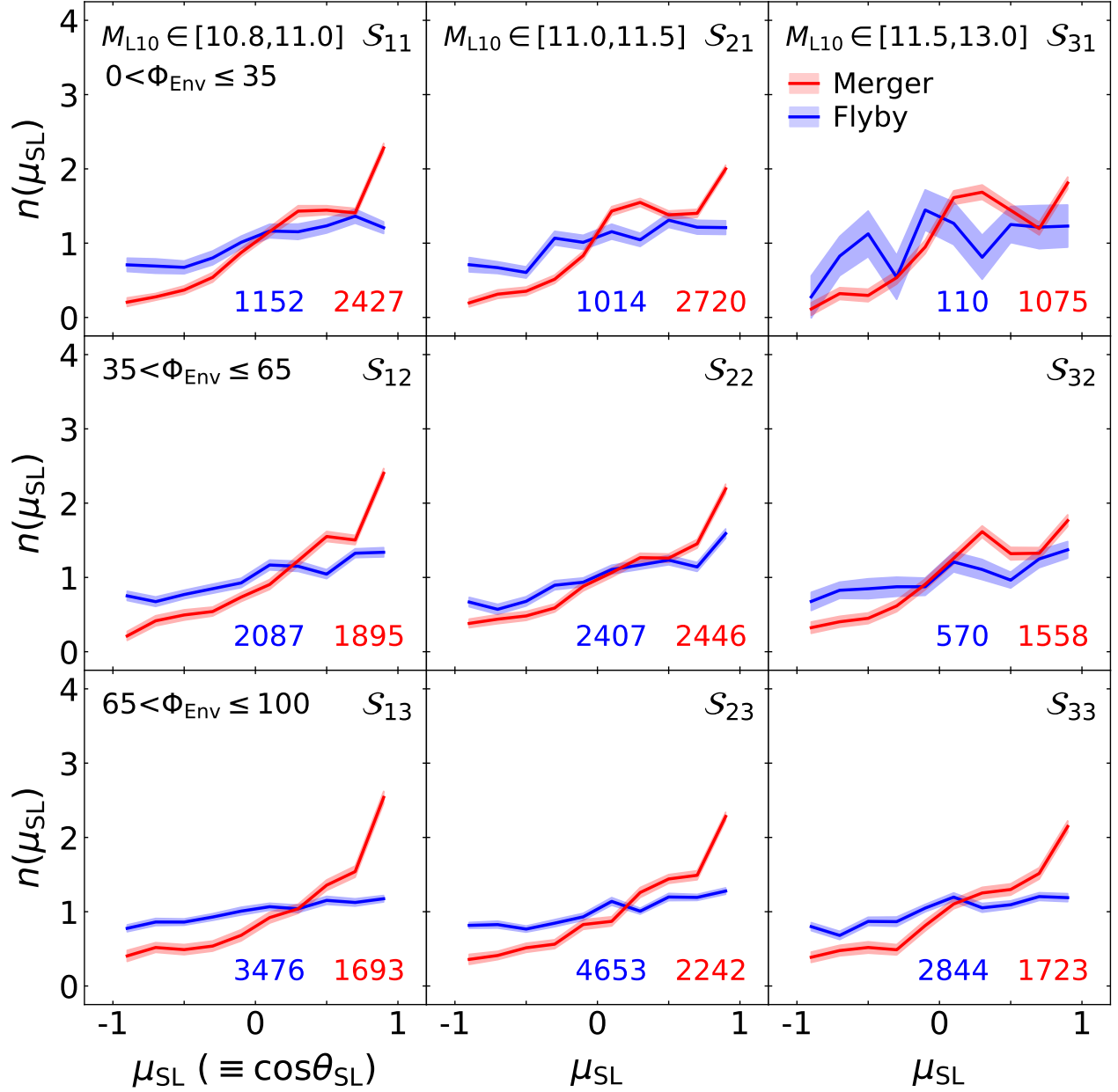


Figure 2. Same as Figure 1, but for merging (red lines) and flybying (blue) neighbors. At the bottom of each panel, we leave numbers of the merging (red) and flybying (blue) neighbors of each subsample (S_{ij}).

$N_{\text{neigh}}(\text{total})$ is the total number of interacting neighbors. The predicted value from the random distribution is 50%. We fit the prograde fractions of subsamples (dotted lines) to assess their mass and environmental dependence using the orthogonal distance regression. To evaluate only the presence or absence of mass and environmental dependence, f_{prog} is described as a simple linear function ($f_{\text{prog}} \propto \beta M_{L10}$ and $\beta \Phi_{\text{Env}}$), where β is the slope of the trends. Table 4 gives the values of β for mass and environmental subsamples.

For given environmental parameters (top panels), the prograde fraction for merging neighbors tends to slightly decrease with increasing halo masses. The mass dependence of f_{prog} is present in the high-density environment at 2.2σ level while becomes insignificant as the density decreases. For flybying neighbors, the significance of the mass dependence is $\leq 1.3\sigma$, and thus the trend of f_{prog} seems constant: f_{prog} is roughly 60% in the low-density environment and 57% in the high-density environment. Overall, the merging neighbors ($75.0 \pm 0.6\%$)

Table 2. Values of n_α in the Merger Subsamples of Figure 2.

Sample	Merging Neighbors				
	$n_{0.1}$	$n_{0.3}$	$n_{0.5}$	$n_{0.7}$	$n_{0.9}$
\mathcal{S}_{11}	1.16 ± 0.06	1.43 ± 0.07	1.44 ± 0.06	1.41 ± 0.06	2.28 ± 0.06
\mathcal{S}_{12}	0.90 ± 0.07	1.23 ± 0.07	1.55 ± 0.07	1.50 ± 0.06	2.40 ± 0.07
\mathcal{S}_{13}	0.92 ± 0.07	1.04 ± 0.06	1.36 ± 0.07	1.54 ± 0.08	2.54 ± 0.08
\mathcal{S}_{21}	1.43 ± 0.06	1.55 ± 0.06	1.38 ± 0.05	1.40 ± 0.05	2.00 ± 0.05
\mathcal{S}_{22}	1.06 ± 0.06	1.27 ± 0.06	1.26 ± 0.06	1.45 ± 0.06	2.19 ± 0.06
\mathcal{S}_{23}	0.87 ± 0.06	1.26 ± 0.07	1.44 ± 0.06	1.49 ± 0.06	2.28 ± 0.06
\mathcal{S}_{31}	1.61 ± 0.09	1.69 ± 0.10	1.44 ± 0.09	1.20 ± 0.09	1.81 ± 0.08
\mathcal{S}_{32}	1.26 ± 0.08	1.62 ± 0.08	1.32 ± 0.09	1.33 ± 0.08	1.77 ± 0.08
\mathcal{S}_{33}	1.10 ± 0.06	1.25 ± 0.08	1.30 ± 0.08	1.52 ± 0.08	2.15 ± 0.08

Notes. Values of n_α are defined by $n(\alpha - 0.1 < \mu_{\text{SL}} < \alpha + 0.1)$ in Equation 2. The error is calculated from 100 random generations. In the \mathcal{S}_{ij} sample, the first and second indices increase with the halo mass and the environmental parameter, respectively.

Table 3. Values of n_α in the Flyby Subsamples of Figure 2.

Sample	Flybying Neighbors				
	$n_{0.1}$	$n_{0.3}$	$n_{0.5}$	$n_{0.7}$	$n_{0.9}$
\mathcal{S}_{11}	1.16 ± 0.09	1.15 ± 0.10	1.23 ± 0.10	1.36 ± 0.09	1.21 ± 0.08
\mathcal{S}_{12}	1.17 ± 0.07	1.15 ± 0.07	1.04 ± 0.06	1.33 ± 0.06	1.34 ± 0.06
\mathcal{S}_{13}	1.07 ± 0.05	1.04 ± 0.05	1.15 ± 0.05	1.12 ± 0.05	1.17 ± 0.04
\mathcal{S}_{21}	1.15 ± 0.10	1.04 ± 0.09	1.31 ± 0.10	1.21 ± 0.09	1.21 ± 0.09
\mathcal{S}_{22}	1.11 ± 0.06	1.17 ± 0.06	1.23 ± 0.06	1.14 ± 0.06	1.59 ± 0.06
\mathcal{S}_{23}	1.14 ± 0.05	1.01 ± 0.04	1.20 ± 0.05	1.19 ± 0.04	1.28 ± 0.04
\mathcal{S}_{31}	1.27 ± 0.29	0.81 ± 0.30	1.25 ± 0.24	1.22 ± 0.29	1.23 ± 0.28
\mathcal{S}_{32}	1.21 ± 0.13	1.11 ± 0.14	0.96 ± 0.11	1.25 ± 0.12	1.37 ± 0.11
\mathcal{S}_{33}	1.20 ± 0.05	1.05 ± 0.06	1.09 ± 0.05	1.20 ± 0.05	1.19 ± 0.05

Notes. Values of n_α are defined by $n(\alpha - 0.1 < \mu_{\text{SL}} < \alpha + 0.1)$ in Equation 2. The error is calculated from 100 random generations. In the \mathcal{S}_{ij} sample, the first and second indices increase with the halo mass and the environmental parameter, respectively.

have a prograde fraction 16.3% higher than that of the flybying neighbors ($58.7 \pm 0.6\%$).

For given halo masses (bottom panels), the prograde fraction mostly decreases for both interaction types as the environment becomes denser (Φ_{Env} increases): f_{prog} for the merging (flybying) neighbors changes from 81% (62%) to 70% (55%). The trend has a higher significance level than 2σ (but 1.5σ for merging neighbors of low-mass target halos and 1.1σ for flybying neighbors of high-mass target halos). Such a decline of the prograde fraction was observed in the more isotropic distribution of satellite galaxies in cluster environments (Wang et al. 2018b). It appears that our result is consistent with the finding of Wang et al. (2018b) because comparable-mass neighbors largely infall into their target halo along the

local tidal field (Tempel & Tamm 2015; Mesa et al. 2018, for galaxies), similarly to low-mass satellites.

3.3. Bump in the Spin-Orbit Angle Distribution

Figure 4 presents the strength of the excess bump as a function of the halo mass (top panels) and the environmental parameter (bottom), to further investigate the occurrence of prograde-polar interactions. We define the excess fraction as

$$f_{\text{exc}}(\%) \equiv \frac{N_{\text{neigh}}(0 < \mu_{\text{SL}} < 0.5)}{N_{\text{neigh}}(\text{total})} \times 100, \quad (5)$$

where $N_{\text{neigh}}(0 < \mu_{\text{SL}} < 0.5)$ is the number of interacting neighbors on prograde-polar orbits. The random distribution should yield 25%. We describe the excess fraction as a function of the halo mass and environment

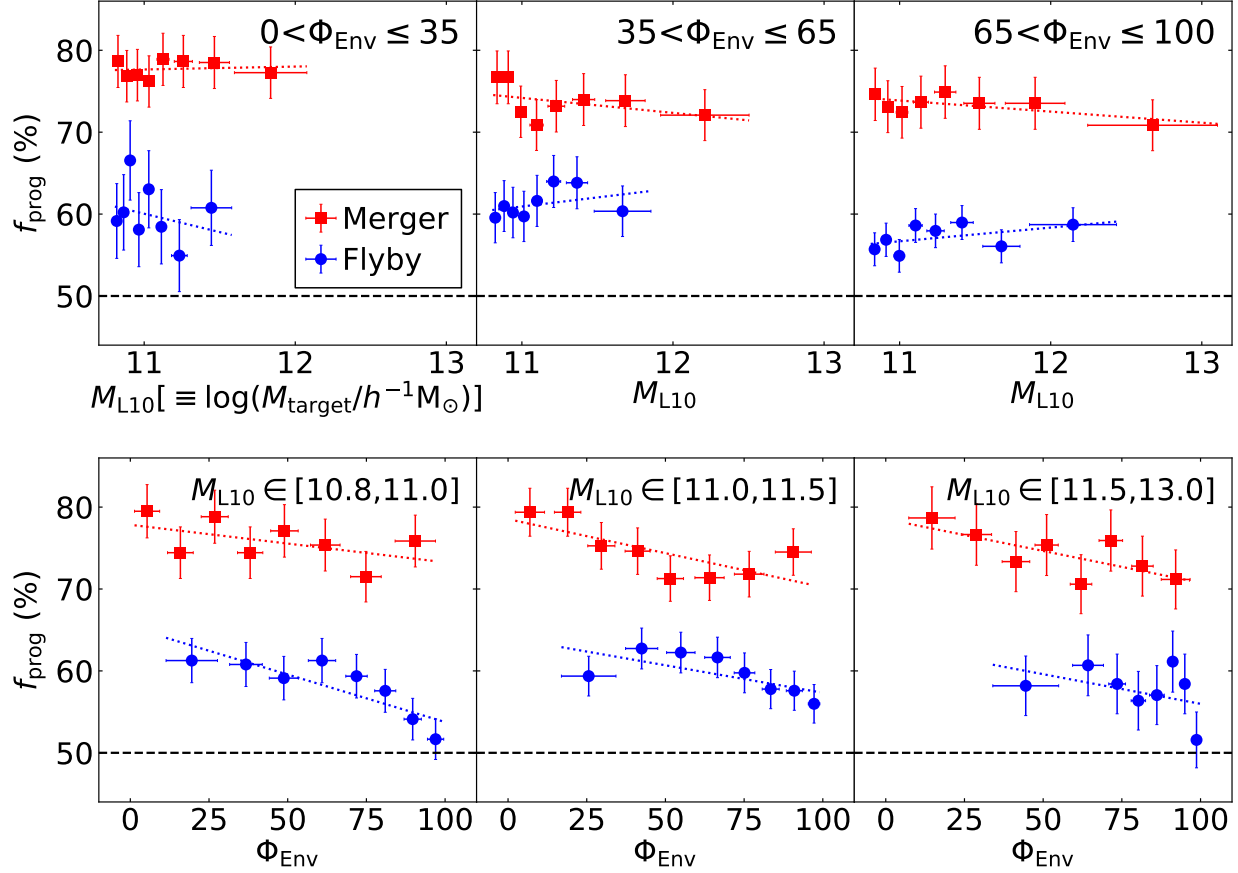


Figure 3. Prograde fraction (f_{prog}) for merging (red squares) and flybying (blue circles) neighbors. Top panels show the prograde fraction as a function of the target halo mass for the three different environmental criteria. Bottom panels show the change of fraction along with the environmental parameter for three different mass samples. In all panels, horizontal dashed lines at $f_{\text{prog}} = 50\%$ indicate the value expected from the random distribution. Error along the x -axis is the standard deviation of subsamples' characteristics of each bin and that along the y -axis is the Poisson error. Dotted lines indicate the linear fit to subsamples using the error-weighted orthogonal distance regression.

Table 4. The Inclination of Mass and Environmental Dependence of Prograde Fraction Presented in Figure 3.

Sample	Inclination β	
	Merger	Flyby
For given environments		
$0 < \Phi_{\text{Env}} \leq 35$	0.354 ± 1.243	-4.487 ± 6.351
$35 < \Phi_{\text{Env}} \leq 65$	-1.830 ± 1.651	2.220 ± 2.293
$65 < \Phi_{\text{Env}} \leq 100$	-1.356 ± 0.630	1.673 ± 1.278
For given halo masses		
$M_{\text{L10}} \in [10.8, 11.0]$	-0.046 ± 0.031	-0.116 ± 0.030
$M_{\text{L10}} \in [11.0, 11.5]$	-0.083 ± 0.032	-0.067 ± 0.029
$M_{\text{L10}} \in [11.5, 13.0]$	-0.078 ± 0.030	-0.072 ± 0.064

Notes. Inclination β is calculated from the linear fit of the prograde fraction with the error-weighted orthogonal distance regression.

via linear fitting. Table 5 displays the inclination of the excess fraction.

First, we examine the mass dependence of f_{exc} . For given environmental parameters (top panels), the excess fraction for the merging neighbors increases with the halo mass. The significance levels of the mass dependence are 5.3σ , 5.0σ , and 3.3σ in the low-, intermediate-, and high-density environments, respectively. The mass dependence of f_{exc} becomes weaker as Φ_{Env} increases. The trend of f_{exc} differs from that of the prograde fraction. In the low-density environment, the mass dependence of f_{exc} is the strongest whereas that of f_{prog} is absent. In the high-density environment, f_{exc} has a tendency opposite to that of f_{prog} . For the flybying neighbors, however, the excess fraction does not show any significant mass dependence. Despite the low significance level ($\sim 1\sigma$), f_{exc} for flybying neighbors seems to depend on the halo mass similarly to that for merging

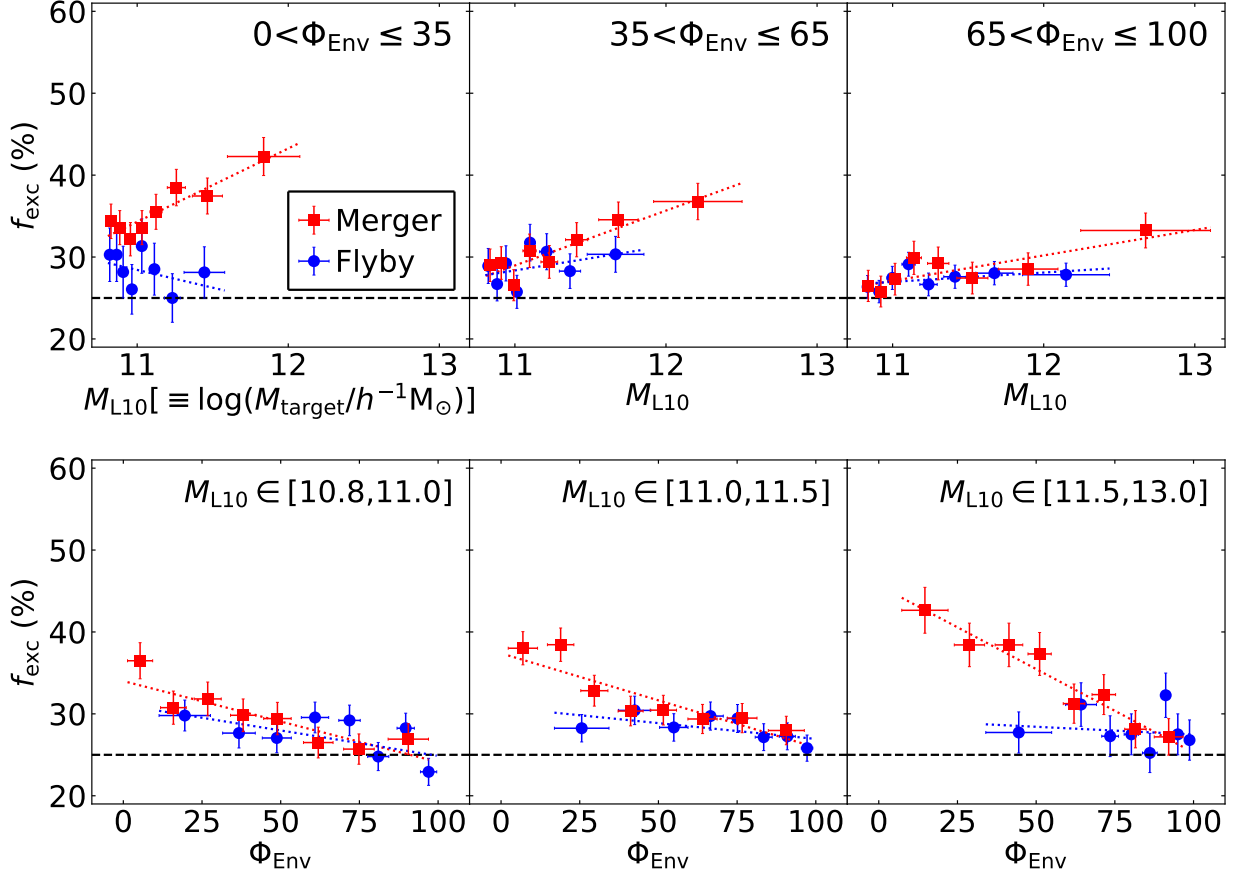


Figure 4. Same as Figure 3, but for the excess fraction (f_{exc}). The horizontal dashed lines at $f_{\text{exc}} = 25\%$ indicate the value expected from the random distribution.

Table 5. The Inclination of Mass and Environmental Dependence of Excess Fraction Presented in Figure 4.

Sample	Inclination β	
	Merger	Flyby
For given environments		
$0 < \Phi_{\text{Env}} \leq 35$	8.959 ± 1.691	-4.341 ± 3.906
$35 < \Phi_{\text{Env}} \leq 65$	6.699 ± 1.340	2.976 ± 2.771
$65 < \Phi_{\text{Env}} \leq 100$	3.107 ± 0.937	1.135 ± 0.859
For given halo masses		
$M_{\text{L10}} \in [10.8, 11.0]$	-0.099 ± 0.022	-0.062 ± 0.030
$M_{\text{L10}} \in [11.0, 11.5]$	-0.115 ± 0.024	-0.039 ± 0.020
$M_{\text{L10}} \in [11.5, 13.0]$	-0.204 ± 0.021	-0.019 ± 0.049

Notes. Inclination β is calculated from the linear fit of the excess fraction with the error-weighted orthogonal distance regression.

neighbors in the intermediate- and high-density environments, but the values of f_{exc} (on average 28%) are quite similar to the value expected from the random distribution.

The mass dependence of f_{exc} for the merging neighbors is most likely associated with the so-called “spin-flip” phenomenon. The spin-flip can be caused by the frequent occurrence of prograde-polar interactions, which incline the halo spin toward a perpendicular direction with respect to its initial angular momentum. According to our results, for more massive halos, f_{exc} increases but f_{prog} decreases. The different trend between two fractions indicates that the prograde-polar interactions ($0 < \mu_{\text{SL}} < 0.5$) become predominant due to a dramatic reduction in frequency of strong-prograde interactions ($0.5 < \mu_{\text{SL}} < 1.0$). Many studies found that the spin-flip happens around a characteristic mass (called the spin-flip mass, $M_{\text{flip}} \simeq 10^{12} h^{-1} M_{\odot}$; e.g., Codis et al. 2012; Ganeshaiah Veena et al. 2018). Our high-mass halo sample covers halos with the spin-flip mass and shows the highest frequency of the prograde-polar interactions. It thus appears that the mass dependence of the spin-flip phenomenon leads to that of f_{exc} .

Second, we examine the environmental dependence of f_{exc} . For given halo masses (bottom panels), the excess fraction decreases with increasing Φ_{Env} , regardless

of the interaction type, except for flybying neighbors of high-mass target halos. For the merging neighbors, f_{exc} decreases from 36 % (43 %) to 27 % (27 %) for the low-mass (high-mass) halos. The decreasing trend has a significance level of $> 4\sigma$ and becomes shallower as the halo mass decreases. For the flybying neighbors, f_{exc} slightly decreases from 29 % to 25 % for the low- and intermediate-mass halos at $\sim 2\sigma$ level. The high-mass halos have insignificant environmental dependence and the mean value of f_{exc} is 27 %. The overall change in f_{exc} for the merging neighbors is larger than that for the flybying neighbors.

The environmental dependence of f_{exc} implies that the cosmic flow perpendicular to the halo spin occurs more in the lower-density environment, due to the anisotropic matter distribution (Libeskind et al. 2011; Shi et al. 2015; Musso et al. 2018). By contrast, the high-density environment corresponds to the knot (node) with a collapsing mode in all directions (Cautun et al. 2014), and thus the cosmic flow is more isotropic in the higher-density environments. The slope is two times steeper in the high-mass halos than in the low-mass halos for the merger sample. This seems to happen because the high-mass range includes the spin-flip mass ($\sim 10^{12} h^{-1} M_{\odot}$). We speculate that most halos with the spin-flip mass in the low-density environment will confront the spin-flip soon.

3.4. Correlation between the Spin–Orbit Alignment and Halo Properties

We examine the correlation of μ_{SL} with relevant parameters in order to figure out what parameter shapes the overall SOA and causes the excess bump in the spin–orbit angle distribution. In Figure 5, we plot the probability map of interacting neighbors on the plane of μ_{SL} versus three quantities: (1) the ratio of the pairwise distance to the virial radius of the target halo ($\gamma_{12} \equiv d_{12}/R_{\text{vir,target}}$); (2) target halo’s triaxiality (Franx et al. 1991), defined as

$$T \equiv \frac{1 - (c/a)^2}{1 - (b/a)^2}, \quad (6)$$

where a , b , and c are the lengths of the major, intermediate, and minor axes, respectively; and (3) target halo’s spin parameter (λ ; Peebles 1969). We contrast the subsample (\mathcal{S}_{31} ; top two rows) having the strongest bump in the distribution with the other subsample (\mathcal{S}_{13} ; bottom two rows) having the weakest bump (see Figure 2). We break the spin–orbit angle distribution into the merger (first and third rows) and flyby samples (second and fourth rows).

In the left column of Figure 5, the median values of μ_{SL} (shown by the dotted lines) tend to decrease with

the increasing pairwise distance ($\gamma_{12} \equiv d_{12}/R_{\text{vir,target}}$) for the merger samples, while the flyby samples show little trend. Namely, the halo spin is preferentially aligned with the orbital angular momentum of the neighboring halo as $\gamma_{12} \rightarrow 0$. The merging companions at $\gamma_{12} < 1$ are mainly on the prograde orbit. We note that the preferential alignment for $\gamma_{12} < 1$ simply implies a positive correlation on the ensemble average at $z = 0$, not the evolution of the spin direction with the pairwise distance. To confirm the time evolution of spins, we should use the merger tree data for each individual halo pair.

In the middle column, the median values of μ_{SL} do not depend on the triaxiality (T) of target halos. The shape dependence of subsamples on μ_{SL} is insignificant, considering the large errors. In the right column, the median values of μ_{SL} increase with the spin parameter λ for the merger samples. The positive correlation of μ_{SL} with the spin disappears for the flybying neighbors. A halo with a high spin ($\lambda > 0.1$) tends to have a merging companion with the orbital angular momentum parallel to the halo spin. For the low-spin counterparts, the two vectors favor being orthogonal. This suggests that the infall direction orthogonal to the spin direction results in the low spin after the merger (Kim et al. 2015).

Our findings indicate that the pairwise distance and spin parameter are involved with the SOA, leading us to further divide the merger and flyby pairs into four subsamples with respect to the two parameters. Now we refer to halos with $\lambda > 0.04$ and $\lambda \leq 0.04$ as fast- and slow-rotating halos, respectively, and neighbors with $\gamma_{12} \leq 1$ and $\gamma_{12} > 1$ as tight and loose neighbors, respectively. Figure 6 shows the μ_{SL} distributions for the four subsamples: (a) fast-rotating halos with tight neighbors (FT), (b) fast-rotating halos with loose neighbors (FL), (c) slow-rotating halos with tight neighbors (ST), and (d) slow-rotating halos with loose neighbors (SL). Tables 6 and 7, respectively, summarize the prograde fraction and the excess fraction for four subsamples (FT, FL, ST, and SL).

Figure 6(a) and Table 6 show, on one hand, that the FT subsample is the main driver behind the prograde alignment of the entire sample as observed back in Figure 2. The values of $n_{0.9}$ for the merging and flybying neighbors of the FT subsample are up to 2.0 times and 1.4 times higher than those for the entire sample, respectively. The strongest prograde alignment of the FT subsample implies that the well-aligned interaction helps the halo spin remain high via the conversion of neighbor’s orbital angular momentum to target halo’s spin (e.g., Aubert et al. 2004; Bailin & Steinmetz 2005). In addition, the bump weakens dramatically for both merging and flybying neighbors. The reduced frequency of

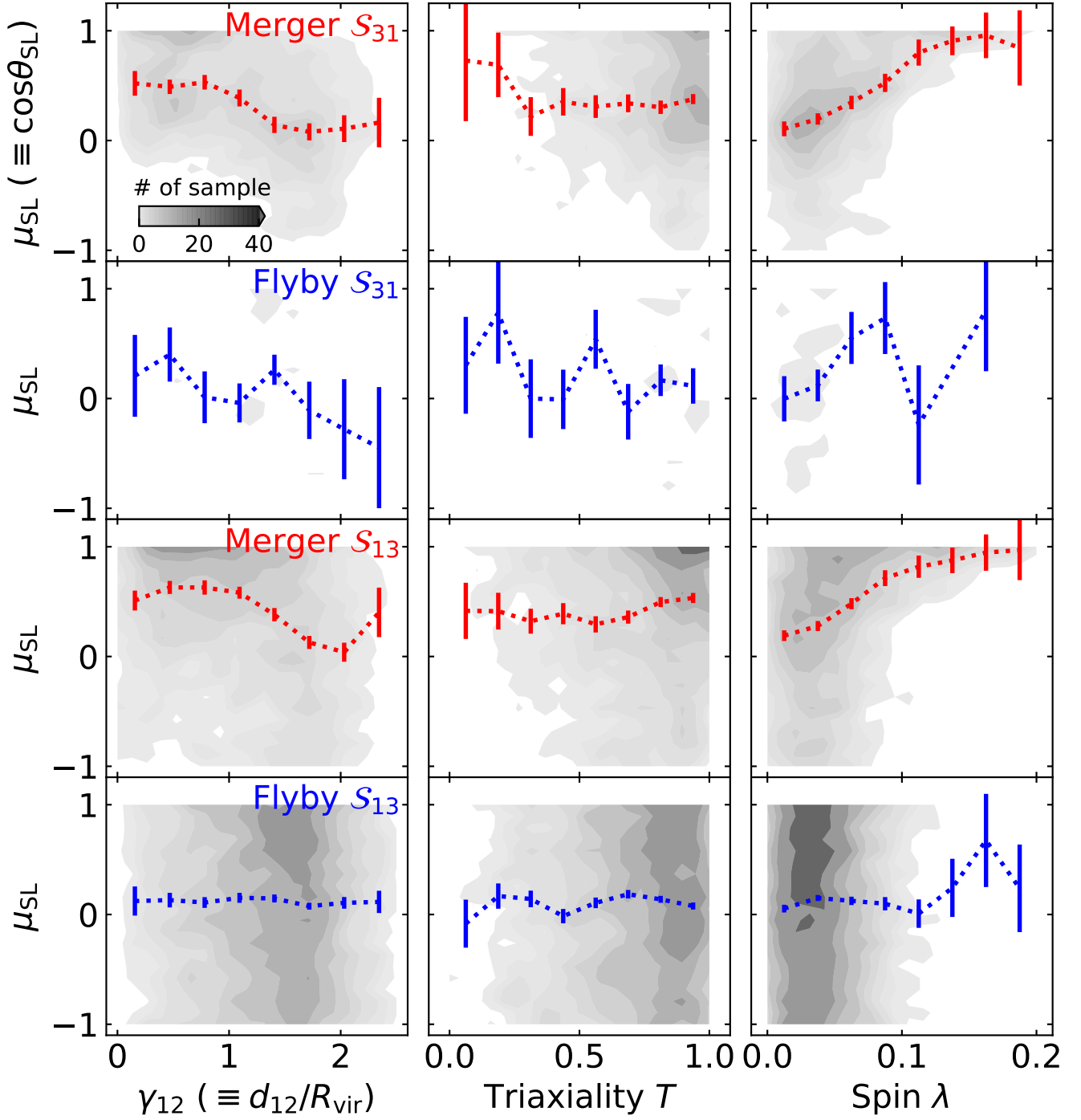


Figure 5. Contour maps of the number of pairs on the plane of μ_{SL} and the properties of pairs or target halos measured from the \mathcal{S}_{31} (top two rows) and \mathcal{S}_{13} (bottom two rows) samples. For the x axis of each column, we adopt the different parameter space as γ_{12} ($\equiv d_{12}/R_{\text{vir,target}}$; the ratio of the pairwise distance (d_{12}) between a target halo and its neighbor to the virial radius ($R_{\text{vir,target}}$) of the target halo), T (triaxiality of the target halo), and λ (spin parameter of the target halo) from the left column, respectively. We select the \mathcal{S}_{31} (having the strongest bump) and \mathcal{S}_{13} (having the weakest bump) samples for a detailed dissection of the bump in the μ_{SL} distribution along these three parameter spaces. First and third rows are for the merging neighbors, and second and fourth rows are for the flybying neighbors. Dotted lines are median values of μ_{SL} in each bin, and their errors are the standard deviations of the median values, which are calculated from 100 random generations.

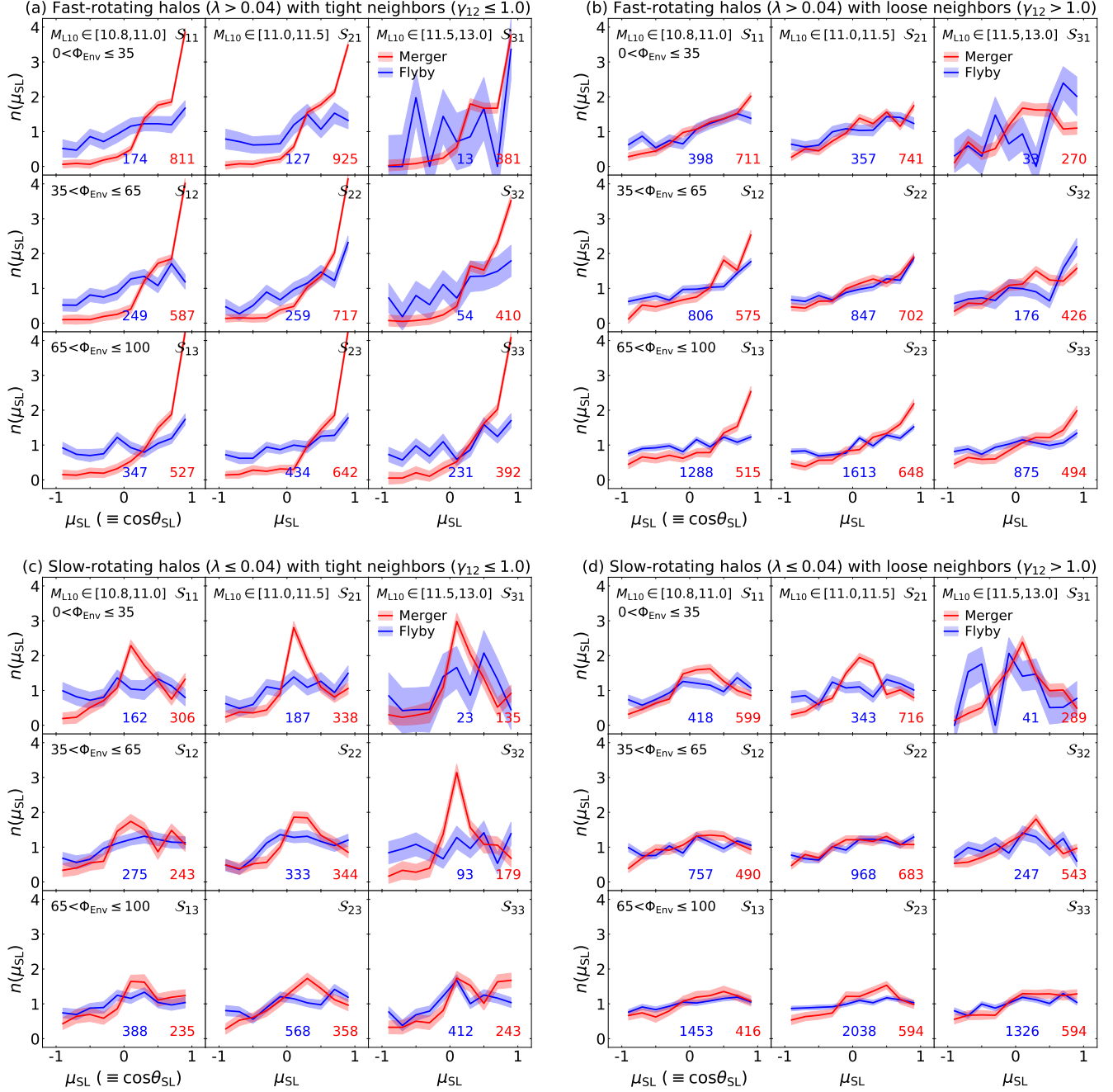


Figure 6. Same as Figure 2, but for (a) fast-rotating halos with tight neighbors ($\lambda > 0.04$ and $\gamma_{12} \leq 1.0$), (b) fast-rotating halos with loose neighbors ($\lambda > 0.04$ and $\gamma_{12} > 1.0$), (c) slow-rotating halos with tight neighbors ($\lambda \leq 0.04$ and $\gamma_{12} \leq 1.0$), and (d) slow-rotating halos with loose neighbors ($\lambda \leq 0.04$ and $\gamma_{12} > 1.0$). In each subsample, λ is the spin parameter of target halos and $\gamma_{12} (\equiv d_{12}/R_{\text{vir,target}})$ is the ratio of the pairwise distance (d_{12}) between a target halo and its neighbor to the virial radius ($R_{\text{vir,target}}$) of the target halo.

Table 6. Prograde Fractions at $z = 0$, Calculated Using the Subsamples of Figure 6.

Sample	Prograde Fraction (%)							
	Fast-rotating Halos				Slow-rotating Halos			
	Tight Neighbors		Loose Neighbors		Tight Neighbors		Loose Neighbors	
	Merger	Flyby	Merger	Flyby	Merger	Flyby	Merger	Flyby
\mathcal{S}_{11}	93 ± 3	66 ± 6	73 ± 3	66 ± 4	73 ± 5	53 ± 6	63 ± 3	58 ± 4
\mathcal{S}_{12}	93 ± 4	65 ± 5	77 ± 4	63 ± 3	66 ± 5	60 ± 5	60 ± 4	56 ± 3
\mathcal{S}_{13}	90 ± 4	57 ± 4	70 ± 4	56 ± 2	68 ± 5	56 ± 4	61 ± 4	55 ± 2
\mathcal{S}_{21}	95 ± 3	66 ± 7	71 ± 3	61 ± 4	77 ± 5	61 ± 6	64 ± 3	54 ± 4
\mathcal{S}_{22}	90 ± 4	72 ± 5	68 ± 3	64 ± 3	71 ± 5	60 ± 4	58 ± 3	60 ± 2
\mathcal{S}_{23}	89 ± 4	62 ± 4	72 ± 3	62 ± 2	67 ± 4	58 ± 3	62 ± 3	54 ± 2
\mathcal{S}_{31}	94 ± 5	62 ± 22	71 ± 5	67 ± 14	77 ± 8	65 ± 17	63 ± 5	46 ± 11
\mathcal{S}_{32}	94 ± 5	67 ± 11	66 ± 4	64 ± 6	74 ± 6	56 ± 8	62 ± 3	55 ± 5
\mathcal{S}_{33}	93 ± 5	60 ± 5	68 ± 4	56 ± 3	76 ± 6	62 ± 4	63 ± 3	56 ± 2

Notes. In the \mathcal{S}_{ij} sample, the first and second indices increase with the halo mass and the environmental parameter, respectively. The error is the statistical Poisson error.

Table 7. Excess Fractions at $z = 0$, Calculated Using the Subsamples of Figure 6.

Sample	Excess Fraction (%)							
	Fast-rotating Halos				Slow-rotating Halos			
	Tight Neighbors		Loose Neighbors		Tight Neighbors		Loose Neighbors	
	Merger	Flyby	Merger	Flyby	Merger	Flyby	Merger	Flyby
\mathcal{S}_{11}	28 ± 2	29 ± 4	30 ± 2	29 ± 3	45 ± 4	28 ± 4	38 ± 3	28 ± 3
\mathcal{S}_{12}	24 ± 2	31 ± 4	26 ± 2	26 ± 2	36 ± 4	31 ± 3	33 ± 3	29 ± 2
\mathcal{S}_{13}	21 ± 2	23 ± 3	23 ± 2	26 ± 1	37 ± 4	31 ± 3	31 ± 3	27 ± 1
\mathcal{S}_{21}	29 ± 2	33 ± 5	34 ± 2	28 ± 3	53 ± 4	30 ± 4	41 ± 2	26 ± 3
\mathcal{S}_{22}	22 ± 2	29 ± 3	31 ± 2	27 ± 2	46 ± 4	32 ± 3	31 ± 2	31 ± 2
\mathcal{S}_{23}	20 ± 2	26 ± 2	27 ± 2	28 ± 1	40 ± 3	27 ± 2	32 ± 2	28 ± 1
\mathcal{S}_{31}	34 ± 3	15 ± 11	40 ± 4	15 ± 7	56 ± 6	43 ± 14	43 ± 4	32 ± 9
\mathcal{S}_{32}	28 ± 3	26 ± 7	32 ± 3	23 ± 4	53 ± 5	33 ± 6	39 ± 3	33 ± 4
\mathcal{S}_{33}	22 ± 2	23 ± 3	29 ± 2	27 ± 2	36 ± 4	33 ± 3	32 ± 2	28 ± 1

Notes. In the \mathcal{S}_{ij} sample, the first and second indices increase with the halo mass and the environmental parameter, respectively. The error is the statistical Poisson error.

the misaligned interaction helps the high halo spin persist. Figure 6(b) displays that the FL subsample shows weaker prograde alignment than the FT subsample does, indicating that the prograde alignment depends on the pairwise distance. This is consistent with the previous findings that the spatial distribution of farther satellites is less aligned with their centrals (Dong et al. 2014; Welker et al. 2017, 2018).

Figure 6(c) and Table 7 show, on the other hand, that the bumps in the μ_{SL} distributions are the most evident in the ST subsample for all masses and environments. It turns out that it is the ST subsample that gives rise to the bump of the entire sample as shown back in Figure 2. For the merging neighbors, the values of $n_{0.1}$ are a

factor of two higher than those for the entire sample. For the flybying neighbors, the enhancement of $n_{0.1}$ is weaker than that for the merging neighbors. Figure 6(d) displays that the SL subsample has the bump as well, but the degree is weaker than that for the ST subsample. Based on Figure 6(c) and (d), we suggest that the slow-rotating halos usually reside in an environment where there is a cosmic flow parallel to their spin. The halos, which formed with the local filament, initially have a spin parallel to the filamentary spine, but soon face the cosmic flow along the filament (Codis et al. 2015). The neighbors following the cosmic flow are candidates for the misaligned interactions, and gradually affect the magnitude and direction of the halo spin (Bett & Frenk

2012, 2016). Moreover, the comparable-mass interacting neighbors with the misaligned orbital angular momentum reduce the halo spin and induce the spin-flip.

In summary, the prograde interaction creates the fast-rotator and the prograde-polar interaction yields the slow-rotator. The halo spin is a product of, at least partially, interactions of neighboring halos. On the other hand, the pairwise distance is a parameter regulating the strength of a feature in the spin-orbit angle distributions. With shorter pairwise distance, both the prograde fraction among the fast-rotators and the excess (i.e., prograde-polar) fraction among the slow-rotating halos tend to enhance greatly.

4. DISCUSSION

4.1. *Validity of Addressing the Spin-Orbit Alignment Using Dark Matter Halos*

The analysis in this paper has focused on the dark matter halos only. Our work is based on and consistent with the previous findings of the Zeldovich collapsing model of the cosmic wall, filament, and cluster (Zel'Dovich 1970; Shandarin & Zeldovich 1989) as well as the spin-flip of galaxies (e.g., Wang & Kang 2017; Welker et al. 2017, 2018). A caveat of this study, however, is that the halo spin can be misaligned with the galaxy spin (e.g., Catelan et al. 2001; Bailin et al. 2005; Shao et al. 2016; Chisari et al. 2017), as mentioned in our Introduction. The degree of galaxy-halo misalignment is as small as 30° for the high-mass halos (Bailin & Steinmetz 2005; Chisari et al. 2017). Moreover, Shao et al. (2016) found that a galaxy whose major axis is well aligned with its satellites' distribution shows tighter galaxy-halo alignment than for the misaligned case. Although they dealt with the satellites rather than comparable-mass neighbors, we can infer that the comparable-mass neighbors should have a similar effect because a halo with a comparable-mass neighbor typically has a high spin (Johnson et al. 2019). Hence, the prograde alignment for dark matter halos is also expected for galaxies.

On the other hand, Shao et al. (2016) found that, with interacting neighbors on the prograde-polar orbit, the halo spin is highly misaligned with the galaxy spin. This is attributed to the fact that the galaxy spin is more vulnerable than the halo spin, due to hydrodynamic effects (such as disk instability and stellar feedback) as well as gravitational effects. The prograde-polar interactions may be less common for galaxies, similarly to the findings of Chisari et al. (2017) and Codis et al. (2018) that the intrinsic alignment for galaxies is weaker than that for dark matter halos. Despite the present galaxy-halo misalignment, the galaxy spin has followed and will be

aligned with the halo spin after all (Okabe et al. 2020). Hence, it is legitimate to address the SOA phenomenon using dark matter halos, and the SOA of halos is crucial in understanding the evolution of the galaxy spin. In an upcoming paper of the present series, we will assess the SOA of galaxies and its evolution using state-of-the-art cosmological hydrodynamic simulations.

4.2. *Implications of the Spin-Orbit Alignment*

We have shown that the halo spin is highly aligned with the orbital angular momentum of a comparable-mass neighbor (see Figure 1). The halo spin seems, to a considerable extent, to be created by the tidal interaction with neighbors. Two interesting facts stick out: (1) merging pairs show stronger SOA than do flybying pairs (see Figure 2); and (2) fast-rotating halos show stronger SOA than do slow-rotating halos (see Figure 6). The implications of the findings are discussed below, one by one.

The stronger SOA for the merging pairs can be attributed to their longer duration of interaction compared to the flybying pairs. The merger exerts a strong tide during an interaction and converts the orbital angular momentum of a neighbor into the spin of its target halo (Hetznecker & Burkert 2006). Such transformation sets the halo spin to align with the orbital angular momentum of the neighbor (Fernando et al. 2017). In the same vein, Cervantes-Sodi et al. (2010) found that the spin directions of two galaxies in a pair are more parallel for the smaller pairwise distance. Lee et al. (2020) showed that paired galaxies with stronger SOA physically resemble each other more (in terms of color) than the other paired galaxies with weaker SOA. By contrast, the flyby has a shorter duration of interaction than the merger (Gnedin 2003; Paper II). Thus, the conversion from the external angular momentum into the internal is limited.

The strong SOA for the fast-rotating halos with close (i.e., tight) neighbors seems to arise from continuous accretion of other halos coming along the cosmic flow. The tidal torque by the primordial density fluctuation regulates the halo spin direction (tidal torque theory; Peebles 1969) to be perpendicular to the cosmic flow (e.g., Wang et al. 2011), and the SOA emerges naturally. Such alignment gets stronger with time by means of interacting with some of the halos that move along the ambient cosmic flow. Tempel & Tamm (2015) and Mesa et al. (2018) observed the orientation of galaxy pairs to be aligned with the spine of the nearest filament, similarly to the spatial distribution of satellite galaxies (Welker et al. 2018). Taken altogether, it is suggested that the prograde interactions along the cosmic flow make the halos spin faster. The fast rotation by the prograde in-

teraction may hold true not only for dark matter halos but for galaxies (Lagos et al. 2018). Especially for a disk galaxy, the continuous prograde accretion is required to maintain the angular momentum of its disk to date (Sales et al. 2012; Peng & Renzini 2020).

4.3. Implications of the Spin-Orbit Misalignment

This paper is the first of its kind to demonstrate the number excess of the prograde-polar interactions ($0 < \mu_{\text{SL}} < 0.5$) in the spin-orbit angle distribution, i.e., the spin-orbit misalignment. The misaligned orbital angular momentum is large enough to dramatically change the spin direction of the halo (Hetznecker & Burkert 2006), causing a spin-flip. The prograde-polar interaction is expected to happen most frequently around the spin-flip mass ($M_{\text{flip}} \simeq 10^{12} h^{-1} M_{\odot}$). This trend can be read from Figure 2. For the bump at a higher mass than ours ($M_{\text{target}} > 10 \times M_{\text{flip}}$), a larger simulation is necessary. However, it is expected that a more massive halo ($M_{\text{target}} > M_{\text{flip}}$) has a more isotropic infall direction that reduces the frequency of perpendicular interactions. It may also be that a more massive halo is unable to recover its original spin direction (parallel to the local filamentary line) after the first spin-flip (Dekel et al. 2020).

The large-scale environment influences the frequency of prograde-polar interactions and thus the spin-flip frequency. The spin-flip mass increases with the large-scale density (Ganeshaiah Veena et al. 2018). If two halos have the same initial masses but reside in different environments, the halo in the less-dense environment has the shorter path of mass growth to M_{flip} . Hence, the change in spin is more dramatic and the frequency of prograde-polar interactions is greater than in the higher-density counterpart.

The prograde-polar interactions are found most frequently among slow-rotating halos, implying that the misaligned interaction reduces the halo spin. Hetznecker & Burkert (2006) found that the halo spin weakens with the total internal energy of the central halo, due to the misaligned orbital angular momenta of satellites. The merging neighbors show a significantly enhanced probability of prograde-polar interactions (Figure 6(c) and (d)), implying that the merger is a primary source of the slow rotator (e.g., Cappellari et al. 2011). The misaligned flyby also affects the direction and magnitude of the halo spin by means of the instantaneous tidal perturbation. We thus conjecture that the interacting neighbors on the prograde-polar orbit will soon flip the spin direction of slow-rotating halos to align with the mean orbital angular momentum of neighbors.

The strong number excess of prograde-polar interactions for the high-mass halos in the Local Group-like environments ($\Phi_{\text{Env}} \sim 15$ based on Karachentsev et al. 2013) gives us a clue to explaining the observed plane of satellites, which is perpendicular to the Galactic disk (Shao et al. 2019, and references therein). If our Galaxy has an increased frequency of perpendicular interactions, the satellite galaxies are in the process of infall along the Local Group filament, and in turn, their orbital angular momenta are perpendicular to the Galactic rotation axis. This is in line with the recent mass accretion along the local filament (Wang & Kang 2018). On the other hand, according to our results, the frequency of the perpendicular interaction depends on the halo spin. Our Galaxy is observed to be slow-rotating ($\lambda_{\text{MW}} \simeq 0.02$; Hernández et al. 2001; Hernandez et al. 2007), and it is consistent with the finding of Cervantes-Sodi et al. (2010) that an interaction with a comparable-mass neighbor reduces the halo spin, although the tidal effect in the Local Group-like environment can enhance the halo spin (Lee & Lemson 2013; Johnson et al. 2019). Hence, our expectation that the Galaxy frequently experiences prograde-polar interactions seems to be reasonable. Observationally, however, the orbital configuration of M31 toward the Milky Way is close to the strong-prograde orbit with respect to the Galaxy, while the orbit of the Galaxy with respect to the M31 is close to the prograde-polar orbit (van der Marel et al. 2012, see also van der Marel et al. 2019). We can thus infer that the satellite galaxies, not M31, will induce the spin-flip of our Galaxy.

4.4. Linking the Spin-Orbit Alignment to the Large-scale Structure

Given that the spin-LSS alignment depends on mass (Aragón-Calvo et al. 2007; Wang & Kang 2017) and environment (Ganeshaiah Veena et al. 2018), the mass and environmental dependence of the SOA hints at its involvement with the spin-LSS alignment. In particular, the strong mass and environmental dependence of the excess fraction (significance level $> 3\sigma$) invokes the spin-flip because the prograde-polar interaction is expected to induce the spin-flip. Moreover, our environmental parameter (Φ_{Env}) shows the correlation with the cosmic web type (see Figure 1 of Paper II and Cautun et al. 2014). We can thus infer the connection of the SOA to the spin-LSS alignment.

In Figure 7, we present a schematic diagram describing how the link between the SOA and the LSS arises depending on the cosmic-web type. We take the tidal torque theory (Peebles 1969) to explain the acquisition of the initial angular momentum. According to that the-

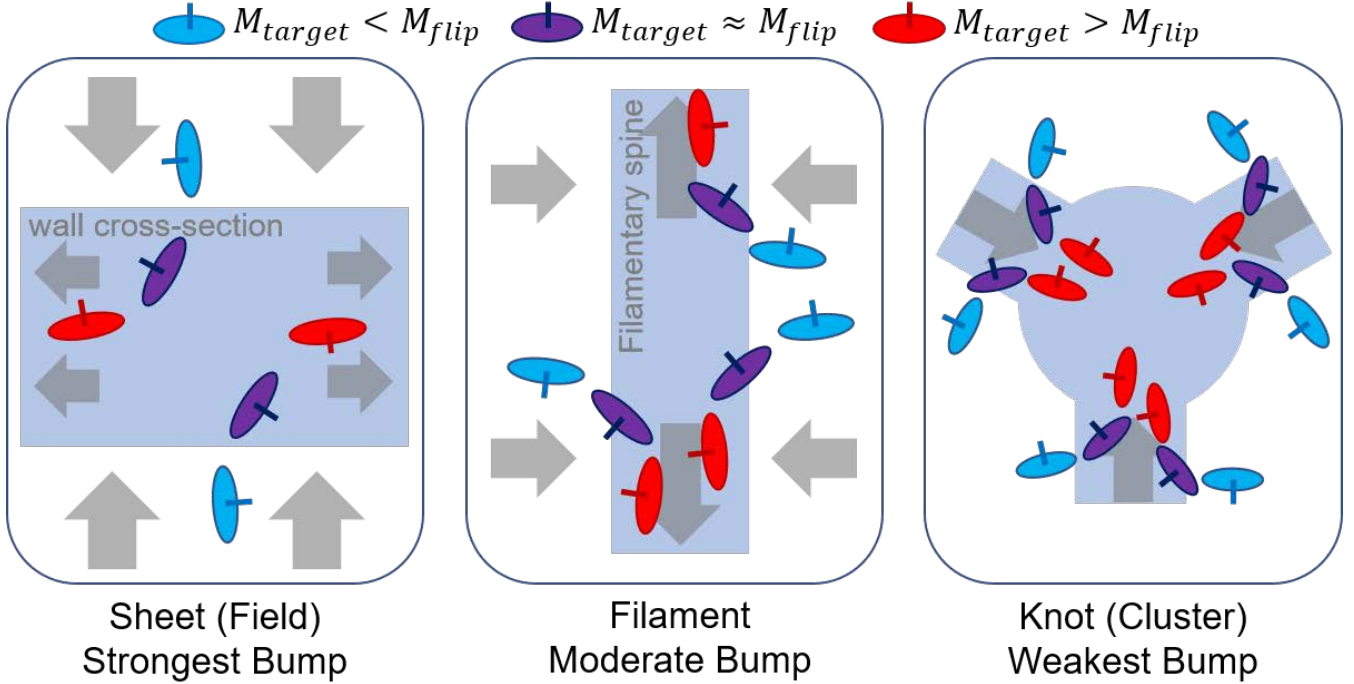


Figure 7. Schematic diagram describing the connection between spin–orbit alignment and large-scale structure (sky-blue) from sheets (left) to filaments (center) and knots (right). Fraction of the prograde-polar interactions is highest in the least dense environment, and lowest in the most dense environment. Colored ellipses indicate the halo mass: blue, purple, and red halos have a mass of $M_{\text{target}} < M_{\text{flip}}$, $M_{\text{target}} \approx M_{\text{flip}}$, and $M_{\text{target}} > M_{\text{flip}}$, respectively. Thick gray arrows describe the dominant matter flows in each large-scale structure.

ory, halos in less dense environments (or cosmic sheets in the Zel'dovich collapsing model; Zel'Dovich 1970; Shandarin & Zel'dovich 1989) first obtain the angular momentum lying on the wall plane or void surface (Lee & Pen 2001; Trujillo et al. 2006; Codis et al. 2015, 2018; see also Varela et al. 2012). With time, however, the direction of the halo spin no longer lies on the wall plane, because the orbital angular momentum of the subsequent infalling matter is normal to the wall plane.

In line with this argument, the spin direction of a halo in sheets or fields deviates from the wall plane as the halo mass grows through accretions and mergers (left panel of Figure 7). Moreover, the direction of the mass accretion depends on the halo mass. Kang & Wang (2015) and Ganeshiah Veena et al. (2018) showed that the direction of matter infalling onto a low-mass halo is usually perpendicular to the wall plane, while for the case of a high-mass halo, the infall mainly happens along the wall plane. By linking the infall direction to the spin, we expect the halos with a mass lower than M_{flip} to show strong prograde alignment. As the halo mass increases, the prograde-polar interactions increase in frequency (top row in Figure 2), and in turn, the SOA becomes weaker. This is because the perpendicular cosmic flow with respect to the wall plane is the strongest even after the spin-flip, and the number excess of prograde-

polar interactions is the strongest in the low-density environment.

In filaments (center panel of Figure 7), the orientation of the halo spin is diverse. In the outskirts of a filament, the spin direction of a less-massive halo ($M_{\text{target}} < M_{\text{flip}}$) tends to be parallel with the filament (Wang & Kang 2018) as the halo moves in the infalling path to the filamentary spine. Hence, the less-massive halo mainly shows a positive prograde alignment ($f_{\text{prog}} \simeq 75\%$), which helps to retain its high spin value. After falling onto the filamentary line, the halo grows in mass and the spin direction changes as matter infalls along the filamentary line (Wang et al. 2005, 2014; Libeskind et al. 2014; Shi et al. 2015; Wang & Kang 2017). This imprints the bump of the prograde-polar alignment in the spin–orbit angle distribution for more massive halos.

In cosmic knots or cluster regions (right panel of Figure 7), the halo spin is almost randomly oriented. In this environment, there is no preferential direction of accretion and mergers, because of the multiple filaments connected to a knot. Wang & Kang (2018) also found that the mass accretion is more isotropic in massive halos. Despite the poor alignment in accretion, the merging neighbors show a noticeable alignment; the prograde fraction for the merging neighbors is approximately 2.3

times higher than the retrograde fraction in the high-density environment. This may be explained by the assumption that merging pairs in clusters had once been in the same filamentary structure and they could retain their binary status even after entering the cluster regions. Kim et al. (2018) confirmed that the Virgo cluster galaxies have a kinematic alignment if they came from the same filament. Although they found alignment between galaxies, it is reasonable to say that our result is consistent with theirs because more massive galaxies are better aligned with their host halos than less massive galaxies (Chisari et al. 2017). Neighbors that came from other filaments would have higher relative velocities and be classified as flybys.

5. SUMMARY

We have investigated the angular alignment between the spin of a target halo and the orbital angular momentum of its neighbor, which we refer to the “spin-orbit alignment (SOA).” Using cosmological dark matter simulations, we have found a strong prograde alignment in the spin-orbit angle distribution and a number excess of the prograde-polar interactions. We have examined the dependence of the SOA on the halo mass, environment, pairwise distance, and the triaxiality and spin of target halos. Our main results are summarized as follows.

- (1) The halo spin is strongly aligned with the orbital angular momentum of the comparable-mass neighbor. The prograde fraction (f_{prog}) is, on average, $75.0 \pm 0.6\%$ for the merging neighbors and $58.7 \pm 0.6\%$ for the flybying neighbors while $f_{\text{prog}} = 50\%$ for the random. The degree of the SOA at $0.8 < \mu_{\text{SL}} (\equiv \cos \theta_{\text{SL}}) < 1.0$ is approximately 120% and 30% higher than the uniform distribution for the merging and flybying neighbors, respectively. The values of f_{prog} marginally decrease with the halo mass for the merging neighbors, but are constant for the flybying neighbors. The mass dependence for the merging neighbors has a significance level of 2.2σ in the high-density environment and becomes weaker as the halo mass increases. The

values of f_{prog} mostly decrease with the large-scale density for both interaction types at a significance level of $> 2\sigma$. The prograde orbit is the most common orbital configuration of the interacting neighbors, because they move along the cosmic flow.

- (2) The excess of prograde-polar interactions ($0.0 < \mu_{\text{SL}} < 0.5$) is substantial in the spin-orbit angle distribution, indicating the frequent occurrence of misaligned interactions. The excess fraction (f_{exc}) for the merging neighbors greatly increases with the halo mass at a significance level of $> 3\sigma$, and decreases with the large-scale density at a significance level of $> 4\sigma$. For the flybying neighbors, the mass and environmental dependence is insignificant. Connected to the spin-LSS alignment, the prograde-polar interaction will flip the halo spin parallel to the local filament toward its perpendicular direction after all.
- (3) The SOA depends on the pairwise distance (γ_{12}) and spin parameter (λ) of target halos, but is independent of the triaxiality (T) of target halos. The prograde-polar interactions show the strongest dependence on λ . Typically, the fast-rotating (slow-rotating) halo has an interacting neighbor whose orbital angular momentum vector is parallel (nearly perpendicular) to the halo spin vector. The strong-prograde (prograde-polar) interaction makes the halo spin faster (slower), implying that tidal interactions with neighbors play a crucial role in the evolution of the halo’s angular momentum.

ACKNOWLEDGMENTS

S.-J.Y. acknowledges support from the Mid-career Researcher Program (No. 2019R1A2C3006242) and the SRC Program (the Center for Galaxy Evolution Research; No. 2017R1A5A1070354) through the National Research Foundation of Korea.

REFERENCES

- Agustsson, I., & Brainerd, T. G. 2010, *ApJ*, 709, 1321
- An, S.-H., Kim, J., Moon, J.-S., & Yoon, S.-J. 2019, *ApJ*, 887, 59
- Aragón-Calvo, M. A., van de Weygaert, R., Jones, B. J. T., & van der Hulst, J. M. 2007, *ApJL*, 655, L5
- Aubert, D., Pichon, C., & Colombi, S. 2004, *MNRAS*, 352, 376
- Bailin, J., & Steinmetz, M. 2005, *ApJ*, 627, 647
- Bailin, J., Kawata, D., Gibson, B. K., et al. 2005, *ApJL*, 627, L17
- Behroozi, P. S., Wechsler, R. H., & Wu, H.-Y. 2013, *ApJ*, 762, 109
- Bennett, C. L., Larson, D., Weiland, J. L., et al. 2013, *ApJS*, 208, 20

- Bett, P., Eke, V., Frenk, C. S., et al. 2007, *MNRAS*, 376, 215
- Bett, P., Eke, V., Frenk, C. S., Jenkins, A., & Okamoto, T. 2010, *MNRAS*, 404, 1137
- Bett, P. E., & Frenk, C. S. 2012, *MNRAS*, 420, 3324
- . 2016, *MNRAS*, 461, 1338
- Blue Bird, J., Davis, J., Lubber, N., et al. 2020, *MNRAS*, 492, 153
- Brainerd, T. G. 2005, *ApJL*, 628, L101
- Buxton, J., & Ryden, B. S. 2012, *ApJ*, 756, 135
- Cappellari, M., Emsellem, E., Krajnović, D., et al. 2011, *MNRAS*, 416, 1680
- Catelan, P., Kamionkowski, M., & Blandford, R. D. 2001, *MNRAS*, 320, L7
- Cautun, M., van de Weygaert, R., Jones, B. J. T., & Frenk, C. S. 2014, *MNRAS*, 441, 2923
- Cervantes-Sodi, B., Hernandez, X., & Park, C. 2010, *MNRAS*, 402, 1807
- Chisari, N. E., Koukoufilippas, N., Jindal, A., et al. 2017, *MNRAS*, 472, 1163
- Codis, S., Jindal, A., Chisari, N. E., et al. 2018, *MNRAS*, 481, 4753
- Codis, S., Pichon, C., Devriendt, J., et al. 2012, *MNRAS*, 427, 3320
- Codis, S., Pichon, C., & Pogosyan, D. 2015, *MNRAS*, 452, 3369
- Darg, D. W., Kaviraj, S., Lintott, C. J., et al. 2011, *MNRAS*, 416, 1745
- Dekel, A., Ginzburg, O., Jiang, F., et al. 2020, *MNRAS*, 493, 4126
- Dong, X. C., Lin, W. P., Kang, X., et al. 2014, *ApJL*, 791, L33
- Dubinski, J., Kim, J., Park, C., & Humble, R. 2004, *NewA*, 9, 111
- Fernando, N., Arias, V., Guglielmo, M., et al. 2017, *MNRAS*, 465, 641
- Forero-Romero, J. E., Contreras, S., & Padilla, N. 2014, *MNRAS*, 443, 1090
- Franx, M., Illingworth, G., & de Zeeuw, T. 1991, *ApJ*, 383, 112
- Ganeshaiah Veena, P., Cautun, M., Tempel, E., van de Weygaert, R., & Frenk, C. S. 2019, *Monthly Notices of the Royal Astronomical Society*, 487, 1607
- Ganeshaiah Veena, P., Cautun, M., van de Weygaert, R., et al. 2018, *Monthly Notices of the Royal Astronomical Society*, 481, 414
- Gnedin, O. Y. 2003, *ApJ*, 582, 141
- Hahn, O., Carollo, C. M., Porciani, C., & Dekel, A. 2007, *MNRAS*, 381, 41
- Herbert-Fort, S., Zaritsky, D., Jin Kim, Y., Bailin, J., & Taylor, J. E. 2008, *MNRAS*, 384, 803
- Hernández, X., Avila-Reese, V., & Firmani, C. 2001, *MNRAS*, 327, 329
- Hernandez, X., Park, C., Cervantes-Sodi, B., & Choi, Y.-Y. 2007, *MNRAS*, 375, 163
- Hetznecker, H., & Burkert, A. 2006, *MNRAS*, 370, 1905
- Hwang, H. S., & Park, C. 2010, *ApJ*, 720, 522
- Johnson, J. W., Maller, A. H., Berlind, A. A., Sinha, M., & Holley-Bockelmann, J. K. 2019, *MNRAS*, 486, 1156
- Kang, X., & Wang, P. 2015, *ApJ*, 813, 6
- Karachentsev, I. D., Makarov, D. I., & Kaisina, E. I. 2013, *AJ*, 145, 101
- Kim, J., Choi, Y.-Y., Kim, S. S., & Lee, J.-E. 2015, *ApJS*, 220, 4
- Kim, S., Jeong, H., Lee, J., et al. 2018, *ApJL*, 860, L3
- Krolewski, A., Ho, S., Chen, Y.-C., et al. 2019, *ApJ*, 876, 52
- Lagos, C. d. P., Stevens, A. R. H., Bower, R. G., et al. 2018, *MNRAS*, 473, 4956
- Laigle, C., Pichon, C., Codis, S., et al. 2015, *MNRAS*, 446, 2744
- Lee, J. 2012, *ApJ*, 751, 153
- Lee, J., & Lemson, G. 2013, *JCAP*, 2013, 022
- Lee, J., & Pen, U.-L. 2001, *ApJ*, 555, 106
- Lee, J. H., Pak, M., & Lee, H.-R. 2020, *ApJ*, 893, 154
- Lee, J. H., Pak, M., Lee, H.-R., & Song, H. 2019a, *ApJ*, 872, 78
- Lee, J. H., Pak, M., Song, H., et al. 2019b, *ApJ*, 884, 104
- L’Huillier, B., Park, C., & Kim, J. 2017, *MNRAS*, 466, 4875
- Libeskind, N. I., Frenk, C. S., Cole, S., et al. 2005, *MNRAS*, 363, 146
- Libeskind, N. I., Knebe, A., Hoffman, Y., & Gottlöber, S. 2014, *MNRAS*, 443, 1274
- Libeskind, N. I., Knebe, A., Hoffman, Y., et al. 2011, *MNRAS*, 411, 1525
- Mesa, V., Duplancic, F., Alonso, S., Coldwell, G., & Lambas, D. G. 2014, *MNRAS*, 438, 1784
- Mesa, V., Duplancic, F., Alonso, S., et al. 2018, *A&A*, 619, A24
- Moon, J.-S., An, S.-H., & Yoon, S.-J. 2019, *ApJ*, 882, 14
- Musso, M., Cadiou, C., Pichon, C., et al. 2018, *MNRAS*, 476, 4877
- Okabe, T., Nishimichi, T., Oguri, M., et al. 2020, *MNRAS*, 491, 2268
- Peebles, P. J. E. 1969, *ApJ*, 155, 393
- Peirani, S., Mohayaee, R., & de Freitas Pacheco, J. A. 2004, *MNRAS*, 348, 921
- Peng, Y.-j., & Renzini, A. 2020, *MNRAS*, 491, L51
- Porciani, C., Dekel, A., & Hoffman, Y. 2002, *MNRAS*, 332, 325

- Rodriguez-Gomez, V., Sales, L. V., Genel, S., et al. 2017, MNRAS, 467, 3083
- Sales, L. V., Navarro, J. F., Theuns, T., et al. 2012, MNRAS, 423, 1544
- Shandarin, S. F., & Zeldovich, Y. B. 1989, Reviews of Modern Physics, 61, 185
- Shao, S., Cautun, M., & Frenk, C. S. 2019, MNRAS, 488, 1166
- Shao, S., Cautun, M., Frenk, C. S., et al. 2016, MNRAS, 460, 3772
- Shi, J., Wang, H., & Mo, H. J. 2015, ApJ, 807, 37
- Stewart, K. R., Brooks, A. M., Bullock, J. S., et al. 2013, ApJ, 769, 74
- Tempel, E., Guo, Q., Kipper, R., & Libeskind, N. I. 2015, MNRAS, 450, 2727
- Tempel, E., & Libeskind, N. I. 2013, ApJL, 775, L42
- Tempel, E., & Tamm, A. 2015, A&A, 576, L5
- Trujillo, I., Carretero, C., & Patiri, S. G. 2006, ApJL, 640, L111
- van der Marel, R. P., Besla, G., Cox, T. J., Sohn, S. T., & Anderson, J. 2012, ApJ, 753, 9
- van der Marel, R. P., Fardal, M. A., Sohn, S. T., et al. 2019, ApJ, 872, 24
- Varela, J., Betancort-Rijo, J., Trujillo, I., & Ricciardelli, E. 2012, ApJ, 744, 82
- Velliscig, M., Cacciato, M., Schaye, J., et al. 2015, MNRAS, 454, 3328
- Vitvitska, M., Klypin, A. A., Kravtsov, A. V., et al. 2002, ApJ, 581, 799
- Wang, H., Mo, H. J., Jing, Y. P., Yang, X., & Wang, Y. 2011, MNRAS, 413, 1973
- Wang, H. Y., Jing, Y. P., Mao, S., & Kang, X. 2005, MNRAS, 364, 424
- Wang, P., Guo, Q., Kang, X., & Libeskind, N. I. 2018a, ApJ, 866, 138
- Wang, P., & Kang, X. 2017, MNRAS, 468, L123
- . 2018, MNRAS, 473, 1562
- Wang, P., Luo, Y., Kang, X., et al. 2018b, ApJ, 859, 115
- Wang, Y., Park, C., Hwang, H. S., & Chen, X. 2010, ApJ, 718, 762
- Wang, Y. O., Lin, W. P., Kang, X., et al. 2014, ApJ, 786, 8
- Welker, C., Dubois, Y., Pichon, C., Devriendt, J., & Chisari, N. E. 2018, A&A, 613, A4
- Welker, C., Power, C., Pichon, C., et al. 2017, arXiv e-prints, arXiv:1712.07818
- Welker, C., Bland-Hawthorn, J., Van de Sande, J., et al. 2020, MNRAS, 491, 2864
- Yang, X., van den Bosch, F. C., Mo, H. J., et al. 2006, MNRAS, 369, 1293
- York, D. G., Adelman, J., Anderson, John E., J., et al. 2000, AJ, 120, 1579
- Zavala, J., Frenk, C. S., Bower, R., et al. 2016, MNRAS, 460, 4466
- Zel'Dovich, Y. B. 1970, A&A, 500, 13
- Zhang, Y., Yang, X., Wang, H., et al. 2015, ApJ, 798, 17
- Zjupa, J., & Springel, V. 2017, MNRAS, 466, 1625